Check for updates

JGR Space Physics

RESEARCH ARTICLE
10.1029/2023JA032151

Propagation of Very Oblique Chorus Waves Near a Plasmaspheric Plume Boundary

Wenyao Gu[1], David Hartley[2], Xu Liu[1], Lunjin Chen[1], Jacob Bortnik[3], and Richard B. Horne[4]

[1]W. B. Hanson Center for Space Sciences, Department of Physics, University of Texas at Dallas, Richardson, TX, USA, [2]Physics and Astronomy Department, University of Iowa, Iowa City, IA, USA, [3]Department of Atmospheric and Oceanic Sciences, University of California, Los Angeles, CA, USA, [4]British Antarctic Survey, Cambridge, UK

Abstract In a case study using Van Allen Probe B, we investigate chorus wave observations near the western edge of a plasmaspheric plume characterized by steep density gradients. Initially, wave vectors are oriented anti-Earthward, but they become very oblique and eastward as the probe approaches the plume boundary. Treating the plume boundary as an azimuthal density gradient, ray tracing can reproduce the observed wave vector directions. Ray tracing shows that the azimuthal density gradient strongly inclines the wave vectors eastward. Consequently, waves are reflected upon reaching the Gendrin angle and cannot enter the plume. We establish an analytical criterion for the azimuthal density enhancement, determining the condition for chorus waves to enter plumes near the equatorial region. Our results partly explain the oblique chorus near plumes observed by Hartley, Chen et al. (2022, https://doi.org/10.1029/2022GL098710), offering insight into wave-particle interactions by chorus waves with the influence of azimuthal density structures.

Plain Language Summary In near-Earth space, whistler-mode chorus waves are typically observed in the plasma trough. The wave vector direction of chorus waves, which is an important parameter in quantifying wave-particle interactions, has been shown to become oblique near the boundaries of plasmaspheric plumes. In this study, we explain this phenomenon by using ray tracing to simulate an observation of chorus waves near a plume boundary with a steep density gradient. Ray tracing shows that the density gradient at the plume boundary can strongly refract the chorus wave, contributing to oblique wave vectors. With a steep density gradient, the wave can be reflected at the plume boundary and thus cannot enter the plume. Our ray-tracing results reproduce the observed wave power distribution in different wave vector directions. We also established an analytical criterion to determine if the chorus wave can enter the plume region near the equatorial region. Our results give insight into wave-particle interactions by chorus waves with the influence of azimuthal density structures such as plume boundaries.

Key Points:

- Chorus waves with very oblique, eastward-oriented k vectors are observed at the westward edge of a plasmaspheric plume
- Ray tracing shows chorus wave vectors are affected by steep azimuthal density gradients, with results being consistent with observations
- A general criterion is established to determine whether chorus can enter plumes, which reveals that entry is not possible in this case

Correspondence to:
W. Gu,
Wenyao.Gu@utdallas.edu

Citation:
Gu, W., Hartley, D., Liu, X., Chen, L., Bortnik, J., & Horne, R. B. (2024). Propagation of very oblique chorus waves near a plasmaspheric plume boundary. *Journal of Geophysical Research: Space Physics*, *129*, e2023JA032151. https://doi.org/10.1029/2023JA032151

Received 5 OCT 2023
Accepted 29 JAN 2024

Author Contributions:
Conceptualization: David Hartley, Lunjin Chen, Jacob Bortnik
Data curation: Wenyao Gu, David Hartley, Xu Liu
Formal analysis: Wenyao Gu, David Hartley, Lunjin Chen
Funding acquisition: David Hartley, Lunjin Chen
Investigation: Wenyao Gu, David Hartley, Lunjin Chen, Jacob Bortnik
Methodology: Wenyao Gu, David Hartley, Xu Liu, Lunjin Chen, Richard B. Horne
Project administration: Lunjin Chen
Supervision: Lunjin Chen
Validation: Wenyao Gu
Visualization: Wenyao Gu, David Hartley
Writing – original draft: Wenyao Gu
Writing – review & editing: Wenyao Gu, David Hartley, Xu Liu, Lunjin Chen, Jacob Bortnik

© 2024. American Geophysical Union. All Rights Reserved.

1. Introduction

Chorus emissions are naturally occurring whistler-mode waves that typically propagate from the magnetic equator to higher latitudes (Burtis & Helliwell, 1969). The emissions are observed in the plasma trough, at all local times but predominantly from the post-midnight to the morning sectors (Agapitov et al., 2018; Meredith et al., 2020). The frequency-time spectrum of chorus emissions includes discrete rising tone or falling tone elements with durations of several 0.1 s (Teng et al., 2017; Xie et al., 2021). A frequency gap is usually present in the spectrum at half of the equatorial electron gyrofrequency and divides the spectrum into an upper band above the gap and a lower band below the gap (Tsurutani & Smith, 1974; Teng et al., 2019; J. Li et al., 2019). Chorus emissions are generated by cyclotron resonance with ~ 10–100 keV electrons with a temperature anisotropy (Omura et al., 2008; Tao, 2014; Trakhtengerts, 1995), typically associated with substorm injections and dayside magnetopause compressions (Ma et al., 2022). The generation region of chorus waves is generally within about 5° magnetic latitude (MLAT) around the magnetic equator (LeDocq et al., 1998; W. Li et al., 2013). Chorus emissions are responsible for interacting with electrons from energies of ~0.1 keV– ~ MeV, including accelerating ~ MeV radiation belts electrons (Horne et al., 2005; Xiao et al., 2014) and scattering electrons into the loss cone, which causes diffuse and pulsating aurora (Nishimura et al., 2011; Thorne et al., 2010) and microbursts (Hikishima et al., 2010; Tsurutani et al., 2013).

In recent decades, the wave normal distribution of chorus has become an interest to scholars (Haque et al., 2010; W. Li et al., 2013; Agapitov et al., 2013; Taubenschuss et al., 2014; W. Li et al., 2016; Agapitov et al., 2018; Shi et al., 2018) due to its controlling role in the energization and scattering rates of electrons (Mourenas et al., 2012;

21699402, 2024, 2, Downloaded from https://agupubs.onlinelibrary.wiley.com/doi/10.1029/2023JA032151 by British Antarctic Survey, Wiley Online Library on [29/09/2025]. See the Terms and Conditions (https://onlinelibrary.wiley.com/terms-and-conditions) on Wiley Online Library for rules of use; OA articles are governed by the applicable Creative Commons License

Shprits & Ni, 2009). At the generation region, there is a group of very oblique, quasi-electrostatic chorus waves whose wave vectors are close to the resonance cone and another group of quasi-parallel chorus waves (Taubenschuss et al., 2014; W. Li et al., 2016). The former group can be generated with anisotropic electron streams (Gao et al., 2016) and would mostly be extinguished at higher latitudes by strong Landau damping (Chen et al., 2013; Lauben et al., 2002). However, oblique lower-band chorus with initial wave normal directed Earthward can survive at high latitudes and become a source of plasmaspheric hiss (Bortnik et al., 2007, 2008, 2009, 2011) or propagate to low latitudes becoming extremely low frequency (ELF) hiss (Santolík et al., 2006). In a smooth background density profile, the quasi-parallel chorus also becomes oblique when propagating to higher latitudes (Burton & Holzer, 1974). Observations support ray-tracing results that the wave normal of the lower band chorus generally inclines in the anti-Earthward direction during propagation (W. Li et al., 2013; Hartley et al., 2019). However, the wave normal may exhibit different behavior in the presence of azimuthal density gradients. A comprehensive review of oblique chorus can be seen in Artemyev et al. (2016).

The chorus obliquity has been shown to significantly increase on both westward and eastward edges of plasmaspheric plumes (Hartley, Chen, et al., 2022). The plasmaspheric plume is a plasmaspheric-like high-density region extended from the main plasmasphere torus (Spasojević et al., 2003), mostly observed from afternoon to evening sectors (Borovsky & Denton, 2008). It is formed during active periods by the strong convection field, which causes a sunward bulge of the plasmasphere (J. Goldstein et al., 2004). The plume bulge can be narrowed and wrapped around the main plasmasphere and rotates eastward (Spasojević et al., 2003; J. Goldstein et al., 2004; Darrouzet et al., 2006). As EUV images show (Figure 5 of Spasojević et al. (2003)), both radial and azimuthal density gradients are presented at both edges of the plume, and the gradient on the westward edge can be more azimuthally directed.

In a statistical survey, Hartley, Chen, et al. (2022) found an eastward skew of wave normal directions of chorus on the eastward edges of plumes, apart from the general anti-Earthward distribution. W. Li et al. (2013) presented a similar phenomenon on a survey of duskside chorus at magnetic latitudes higher than 10°. To explain the cause, Hartley, Chen, et al. (2022) discussed that wave refraction by azimuthal density gradients results in the eastward wave normals. However, a more detailed investigation is required to confirm this statement and quantify the effects of the azimuthal density gradients on chorus propagation, especially on its contribution to the very oblique chorus. In addition, ray-tracing studies showed that the plume can act as an entrance for chorus waves to propagate into the plasmasphere and become hiss emissions because the wave can be directed azimuthally into the plume by the azimuthal density gradients (Chen et al., 2009; Hartley et al., 2019). Any waves that enter the plume may then be guided to the core of the plasmasphere (Wu et al., 2022). As both studies use the same density model (Chen et al., 2009; Hartley et al., 2019), the impact of different plume density profiles on the entry of chorus into the plume and plasmasphere requires further attention.

In this paper, we present a case study of chorus waves observed close to a plume edge. We analyze the wave normal directions of the chorus and use ray tracing to show how the azimuthal density gradient of the plume edge affects the wave normal and wave propagation. The criterion for a plume entry is also discussed. The paper is organized as follows: Section 2 presents the observation of chorus waves. Section 3 performs ray tracing with individual rays and investigates their characteristics. Section 4 applies a bulk of rays to simulate the observations. Section 5 discusses the criterion for plume entry.

2. Observations

Figure 1 presents an observation by Van Allen Probes B on 2017/10/11 from 18:13 to 18:19. The black line in Figure 1a shows the electron density obtained from the upper hybrid resonance line observed by the High-Frequency Receiver (HFR) (Kurth et al., 2015). The satellite encountered a plasmaspheric plume at around 18:18 at L = 5.28, exited the plume at around 18:29 at L = 5.07, and entered the plasmasphere at around 19:21 at L = 3.77. Figure 1b shows the westward edge of the plume (shaded region in Figure 1b). The plume has a steep westward edge where the electron density increases by a factor of 9 from 18:17:15 (hh:mm:ss) to 18:18:07 within ~150 km (Figure 1b). From 18:18:01, the density increases 80 cm^{-3} between adjacent observations (6 s cadence) in 18 km (Figure 1b). Figures 1c and 1d shows magnetic and electric power spectra using Electric and Magnetic Field Instrument Suite and Integrated Science (EMFISIS) Wave Frequency Receiver (WFR) survey data (Kletzing et al., 2013, 2023). Prior to encountering the plume edge, lower band chorus waves were observed from ~150 to ~900 Hz. At the plume edge after 18:17:21, the magnetic power decreases (Figure 1c) while the electric

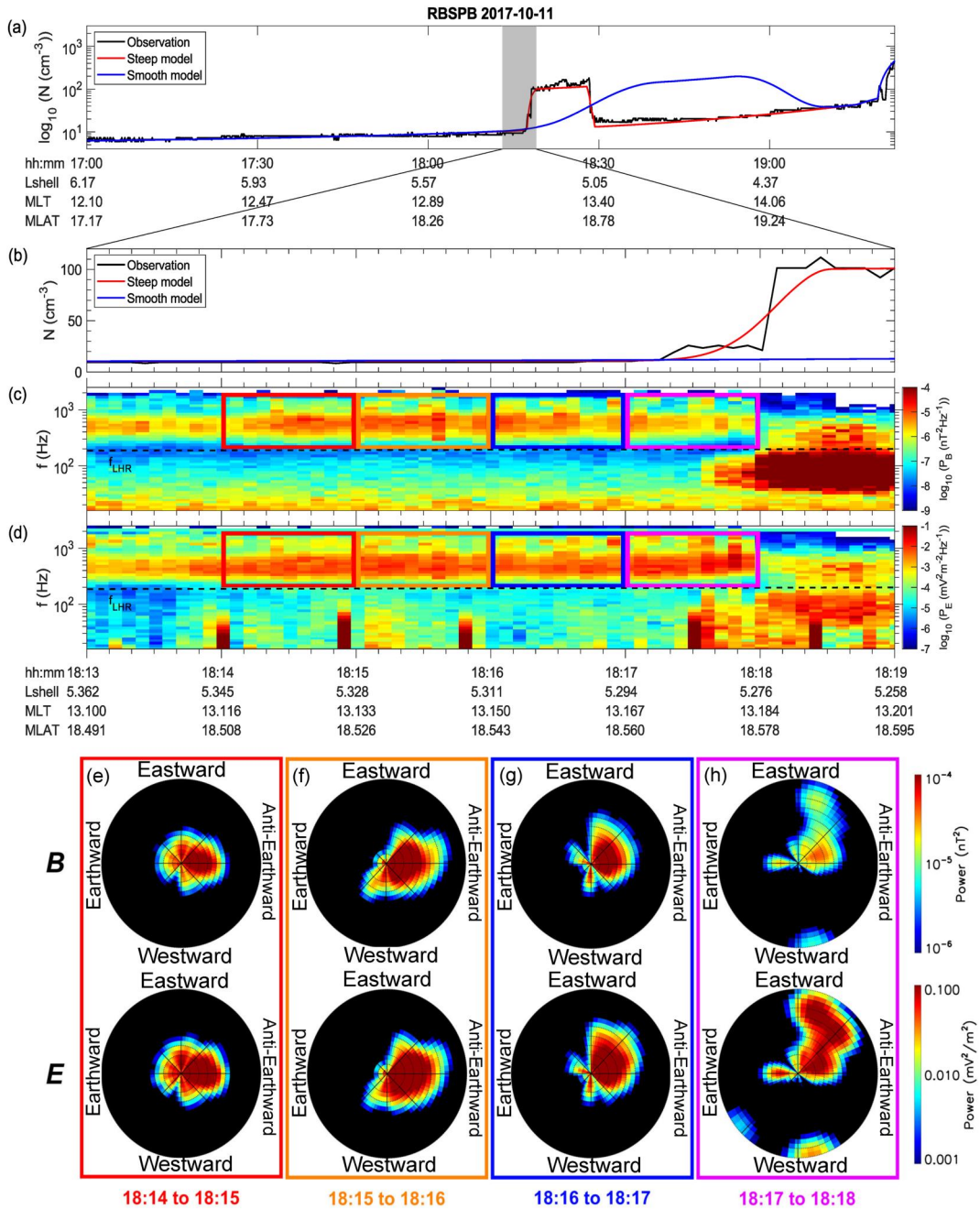

Figure 1. Chorus observation close to the westward edge of a plume and its wave normal distribution. (a) Electron number density in a prolonged time window. The black line indicates the observed density. The red line shows the ray-tracing model density with a steep plume edge density gradient along the satellite's trajectory. The blue line shows the model density with a smooth plume edge. The gray-shaded region is panels (b)–(d) time window. (b) Electron number density. The black dashed line denotes the lower hybrid frequency. (c) Magnetic power spectral density. (d) Electric power spectral density (e)–(h) The distribution of wave power as a function of wave normal directions in θ and ϕ for the four boxes shown in Panels (c) and (d), respectively. The upper plots show the magnetic power distribution and the lower plots show the electric power distribution.

power increases (Figure 1d), which indicates that the wave becomes more electrostatic. The high wave power terminates at the sharp plume boundary at 18:18:01.

To investigate the chorus wave normal directions, we divide the chorus wave spectrum from 18:14 (hh:mm) to 18:18 into four boxes, each of which is 1 min long. The singular value decomposition (SVD) method with three

21699402, 2024, 2, Downloaded from https://agupubs.onlinelibrary.wiley.com/doi/10.1029/2023JA032151 by British Antarctic Survey, Wiley Online Library on [29/09/2025]. See the Terms and Conditions (https://onlinelibrary.wiley.com/terms-and-conditions) on Wiley Online Library for rules of use; OA articles are governed by the applicable Creative Commons License

21699402, 2024, 2, Downloaded from https://agupubs.onlinelibrary.wiley.com/doi/10.1029/2023JA032151 by British Antarctic Survey, Wiley Online Library on [29/09/2025]. See the Terms and Conditions (https://onlinelibrary.wiley.com/terms-and-conditions) on Wiley Online Library for rules of use; OA articles are governed by the applicable Creative Commons License

orthogonal magnetic field components (Santolík et al., 2003) is used for the wave normal analysis. To obtain reliable wave normal estimates requires a power spectral density larger than 10^{-7} nT^2/Hz, a planarity higher than 0.5, and an ellipticity higher than 0.5 in each $f-t$ bin (Hartley et al., 2018, 2019). For data that meet the above criteria, a wave normal direction for each time-frequency bin of the power spectrum is obtained. Figures 1e–1h show the angular distribution of magnetic and electric wave power in each box which satisfies the above criteria in polar coordinates of wave normal angle θ and azimuthal angle of k vector ϕ. The polar axis is arranged as the pole at $\theta = 0°$ and the boundary of the plots at $\theta = 90°$. Note that the SVD method assumes the presence of a plane wave, although the SVD procedure provides reasonable results also for lower planarity cases (Santolík et al., 2003). In an attempt to account for these lower planarity cases, we assume each time-frequency observation to be a Gaussian distribution of wave power centered on the SVD-determined wave normal direction with polar and azimuthal widths of $\Delta\theta = \Delta\phi = 20°$, following Hartley et al. (2019). The angular distribution of wave power is obtained by summing over all frequency-time data contained within each colored box. For the observations presented here, note that the sheath corrected electric field data are used (Hartley, Christopher, et al., 2022b; Hartley et al., 2023). In the first three boxes (red, orange, and blue boxes), which are relatively far away from the plume, most chorus wave power is distributed at anti-Earthward k directions with quasi-parallel wave normal angles between 10° and 40° (Figures 1e–1g). These results are consistent with a quasi-parallel chorus source centered at $\theta = 0°$ and propagation to higher latitudes (at MLAT = 18.5° at the satellite position) where the wave normal direction inclines anti-Earthward because of the magnetic field gradients and curvature (Chen et al., 2013; Hartley et al., 2019). The electric and magnetic power distributions in the first two (red and orange) boxes are approximately east-west symmetric (Figures 1e and 1f), implying that sources are distributed evenly in the East-West direction. In the third (blue) box, the power is mainly distributed eastward (Figure 1g), which implies that the sources are mainly to the west of the third box. In the last (magenta) box just at the plume edge, a quasi-electrostatic power occurs with oblique wave normal angles (50° and 80°) along the eastward direction (Figure 1h). Its magnetic power is significantly smaller than the former three boxes, while the electric power has comparable intensity. In contrast, all the quasi-parallel powers in the former three boxes are electromagnetic waves (Figures 1e–1g). Some of these very oblique waves may have wave normal angles close to or exceeding the Gendrin angle θ_G, where the group velocity becomes parallel to the background magnetic field (Gendrin, 1961). The local Gendrin angle is about 83.5° at 500 Hz and about 77.6° at 900 Hz using the cold plasma dispersion relation (Stix, 1992). In the next two sections, we will conduct a ray tracing analysis in order to investigate the propagation of the chorus based on this observation case.

3. Individual Ray Tracing

In this section, we use the ray-tracing method to study how the azimuthal density gradient of a plume edge can affect the properties of chorus waves. The three-dimensional ray-tracing code HOTRAY (Horne, 1989) is used, and a dipole magnetic field is applied. The base of the density model chosen for the observation is from an azimuthal symmetric model of (Bortnik et al., 2011), consisting of a diffusive equilibrium base and a set of additional field-aligned structures. We set the model parameters to fit the observational density in the plasma trough in Figure 1a as we choose $T_{de} = 1800\text{K}$, $N_b = 7 \times 10^9 m^{-3}$, and $L_p = 3.60$, while setting other parameters the same as the typical nightside values (Bortnik et al., 2011). In addition, we add a purely azimuthal density structure to the model base to focus on the azimuthal gradient's effects. Although both radial and azimuthal density gradients are likely to coexist in the actual scenario, there is no way to verify this with a single spacecraft point measurement. The density structure along magnetic local time (MLT) contains a plateau with half-Gaussian-shaped edges. The density models with the presence of an azimuthal density structure are expressed as:

$$N = \begin{cases} N_b + (a-1)N_b \exp\left(\dfrac{\left(T - T_0 + \frac{1}{2}T_p\right)^2}{2\Delta T^2}\right), & T \le T_0 - \dfrac{1}{2}T_p \\ aN_b, & T_0 - \dfrac{1}{2}T_p < T < T_0 + \dfrac{1}{2}T_p, \\ N_b + (a-1)N_b \exp\left(\dfrac{\left(T - T_0 - \frac{1}{2}T_p\right)^2}{2\Delta T^2}\right), & T \ge T_0 + \dfrac{1}{2}T_p \end{cases} \quad (1)$$

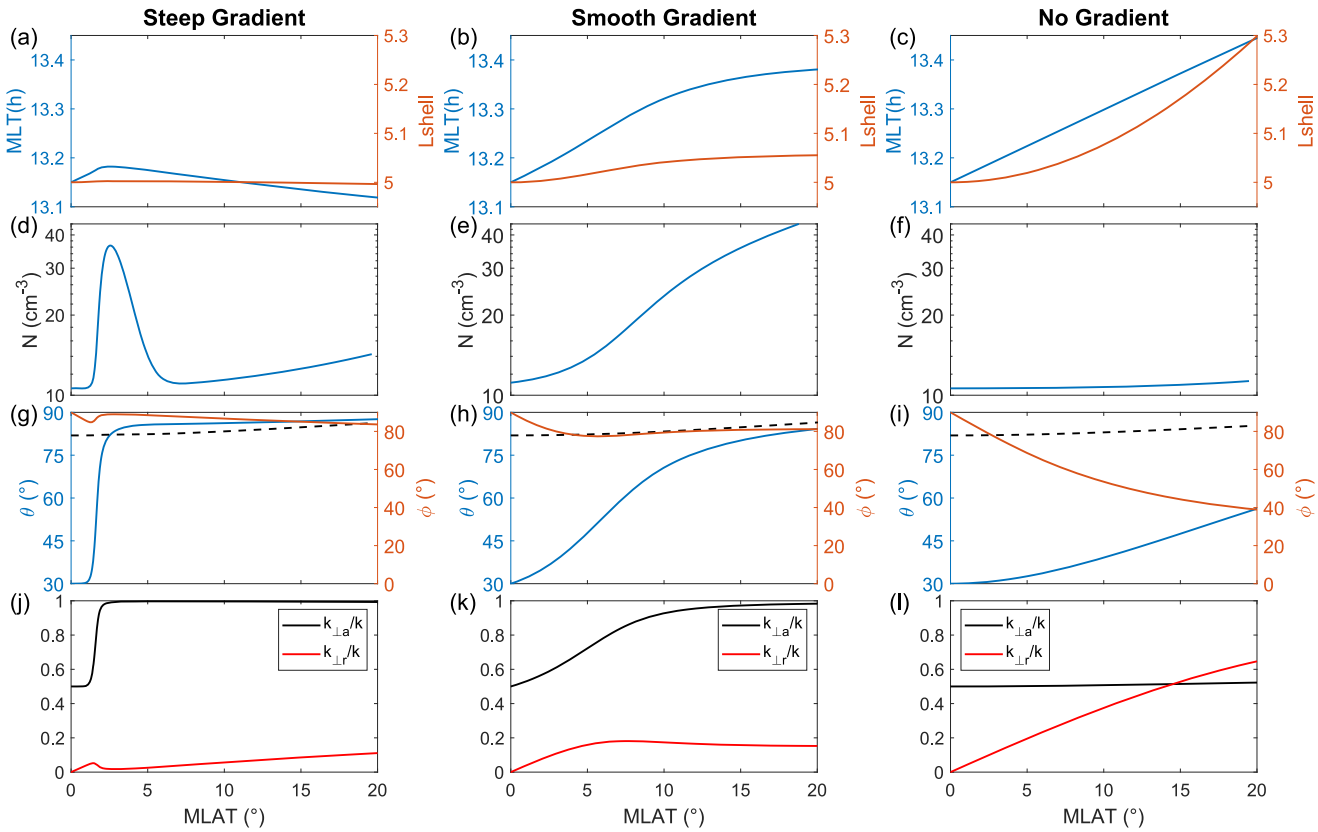

Figure 2. Results of tracing a single ray starting at MLT = 13.150 hr of initial $\theta_0 = 30°$ and $\phi_0 = 90°$ (eastward) in different density models. (a)–(c) Magnetic local time (blue) and L shell (orange) of the ray in the steep density gradient model (left), the smooth density gradient model (middle), and the model with no azimuthal density gradient (right). (d)–(f) Electron density at the ray's location. (g)–(i) Wave normal angle θ (blue) and azimuthal angle of k vetor ϕ (orange) of the ray. The black dashed line shows the local Gendrin angle (j)–(l) $k_{\perp a}/k$ (black) and $k_{\perp r}/k$ (red) of the ray.

where N_b is the model base without the azimuthal density structure, a is the enhancement factor from background density, T_0 is the central MLT of the structure, T_p is the plateau width, and ΔT is the Gaussian half-width of the edges. A steep-density structure is used to fit the observed plume density with an enhancement factor of $a = 9$ and a steep edge with $\Delta T = 0.01$ hr in local time. The structure is located at $T_0 = 13.277$ hr with a plateau width of $T_p = 0.084$ hr. The density along the satellite trajectory of this steep density model is shown in the red lines of Figures 1a and 1b, and the equatorial density is shown by grayscale in Figure 3a. To analyze the effects of different azimuthal density gradients, we create a smooth density model shown in the blue lines of Figures 1a and 1b and the grayscale map in Figure 3b. For comparison purposes, the smooth density model has the same peak density enhancement ($a = 9$) but a relatively smooth edge with $\Delta T = 0.20$ hr. The smooth density structure is located at $T_0 = 13.750$ hr with a plateau width of $T_p = 0.15$ hr. The local times where the azimuthal density enhancement reaches 1% of the peak enhancement value are set as the same in the two models.

To evaluate the effects of azimuthal density gradients on rays, a single ray is launched from the equator at L = 5.0 and MLT = 13.150 hr, which is at the position between the second (orange) and the third (blue) boxes in Figure 1c. We choose the initial L shell as 5.0 (compared to L = 5.3 at the observation) to account for the general anti-Earthward propagation of rays (Chen et al., 2009). The initial value of the wave normal angle is $\theta_0 = 30°$, and the perpendicular component of the k vector is at azimuthal eastward so that the ray would move toward the plume. The results of the ray properties in the steep model (left), the smooth model (middle), and the model base with no azimuthal structure (right) are shown in Figure 2. In the steep density model similar to the realistic plume, the eastward ray encounters the plume edge with a significant density enhancement from 11 cm^{-3}–36 cm^{-3} at MLAT ~ 2° (Figure 2d). Figure 2g shows the wave normal angle θ and the azimuthal angle of k vector ϕ, where $\phi = 0°$ means radially anti-Earthward and $\phi = 90°$ means azimuthally eastward. The wave normal angle θ increases abruptly above 80° while the azimuthal angle perturbs but still stays close to 90° eastward, which aligns

21699402, 2024, 2, Downloaded from https://agupubs.onlinelibrary.wiley.com/doi/10.1029/2023JA032151 by British Antarctic Survey, Wiley Online Library on [29/09/2025]. See the Terms and Conditions (https://onlinelibrary.wiley.com/terms-and-conditions) on Wiley Online Library for rules of use; OA articles are governed by the applicable Creative Commons License

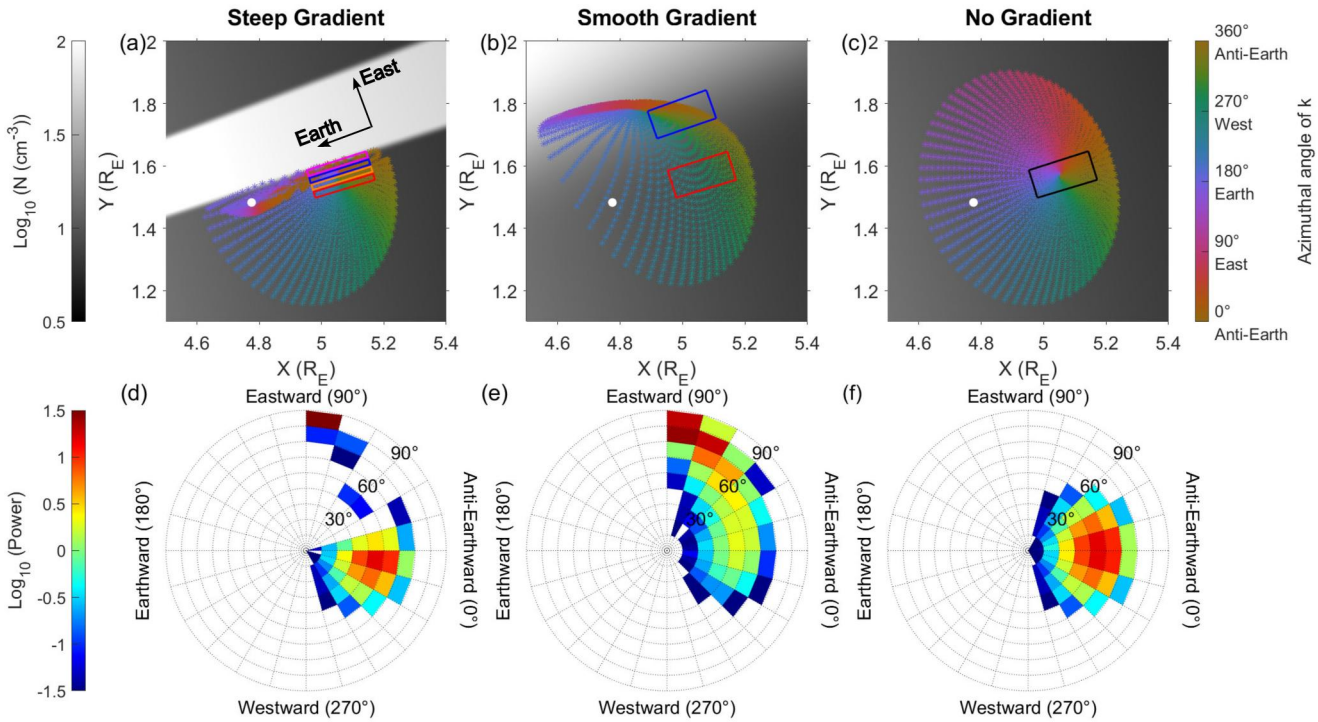

Figure 3. Results of tracing a bulk of rays from a single source at MLT = 13.150 hr (a)–(c) Scatter plots of the equatorial projection locations of the rays at MLAT = 18° in the steep density gradient model (left), the smooth density gradient model (middle), and the model with no azimuthal density gradient (right). The colors of the scattered stars indicate the azimuthal angles of k vectors ϕ. The white dot shows the source location. The grayscale backgrounds show the equatorial density distribution. The colored boxes are used to plot the ray power distributions at MLAT = 18° in Figure 4. (d)–(f) Power distributions of the rays in the three density models at MLAT = 18° as a function of θ and ϕ.

more closely to the very oblique eastward peak in Figure 1h. Figure 2j shows the normalized azimuthal perpendicular component of k vector $k_{\perp a}/k$ in black and the normalized radial perpendicular component of k vector $k_{\perp r}/k$ in red. After the plume encounter, the azimuthal component far exceeds the radial component of the k vector. The ray experiences a reflection at the plume from eastward in MLT to westward (Figure 2a). The reflection is because the wave normal angle has exceeded the Gendrin angle (black dashed line in Figure 2g), and the perpendicular components of the Poynting vector and the k vector become in the opposite directions (Hartley et al., 2023; Helliwell, 1965; Taubenschuss et al., 2016). The reflection observed in the ray tracing results may explain the chorus cut-off at the plume edge (Figures 1c and 1d), as the ray does not enter the plume from the trough. In contrast, the ray in the smooth density model keeps moving eastward into the "smoothed" plume (Figure 2b) during MLAT <20°. The density at the ray keeps increasing (Figure 2e). The ray can still become very oblique but the wave normal angle has not reached the Gendrin angle (Figure 2h). The k vector is majorly directed azimuthally eastward (Figure 2k). For the ray in the model with no azimuthal gradient, the increase of θ is much smaller (Figure 2i). The increase of $k_\perp$ is from the radially anti-Earthward direction rather than the azimuthal direction (Figure 2l). As a result, the $k_\perp$ is directed from azimuthally eastward ($\phi = 90°$) toward radially anti-Earthward ($\phi = 0°$) (Figure 2i) and the ray moves to higher L-shells (Figure 2c). In contrast, the ray in other models remains at roughly the same L shell (Figures 2a and 2b).

4. Ray-Tracing With a Bulk of Rays

The section above shows that a quasi-parallel ray ($\theta_0 = 30°$) can be significantly affected by azimuthal density gradients. In this section, by tracing a bulk of rays, we demonstrate the effect of azimuthal density gradients on a quasi-parallel wave source with a distribution of initial wave vector directions. For chorus waves of quasi-parallel generation, the wave growth is maximum at the parallel direction (B. E. Goldstein & Tsurutani, 1984), and the values of θ at the source region are typically within 30° from observation (W. Li et al., 2016) and within 20° from simulation (Lu et al., 2019). Therefore, we set the launched ray distribution to have initial wave normal angle θ_0

21699402, 2024, 2, Downloaded from https://agupubs.onlinelibrary.wiley.com/doi/10.1029/2023JA032151 by British Antarctic Survey, Wiley Online Library on [29/09/2025]. See the Terms and Conditions (https://onlinelibrary.wiley.com/terms-and-conditions) on Wiley Online Library for rules of use; OA articles are governed by the applicable Creative Commons License

21699402, 2024, 2, Downloaded from https://agupubs.onlinelibrary.wiley.com/doi/10.1029/2023JA032151 by British Antarctic Survey, Wiley Online Library on [29/09/2025]. See the Terms and Conditions (https://onlinelibrary.wiley.com/terms-and-conditions) on Wiley Online Library for rules of use; OA articles are governed by the applicable Creative Commons License

from 1° to 30° with a 1-degree resolution, and for each wave normal angle, 72 rays are evenly distributed along the azimuthal direction. We choose the initial power per solid angle as a Gaussian distribution centered at initial wave normal angle $\theta_0 = 0°$. The initial power of each ray is set as $P_0(\theta_0) = \exp\left(-\theta_0^2/\theta_w^2\right)\sin(\theta_0)$, where the Gaussian width $\theta_w = 15°$. The rays' source is located at MLT = 13.150 hr and L shell = 5.0. We calculate each ray's total gain/loss along the raypath as $\Gamma(s) = \int_0^s \frac{\gamma(f_e,\theta)}{|v_g|} ds'$ (Huang & Goertz, 1983), where v_g is the group velocity and ds' is the spatial integration step along the ray. The temporal linear growth rate γ is calculated as a function of the electron distribution function f_e and wave normal angle θ using Equation 6 in Liu and Chen (2019). f_e is derived from the averaged phase space density from 18:14 (hh:mm) to 18:18 fitted by the energy channels from 25 eV to 51 keV (Liu et al., 2021) observed by the Helium, Oxygen, Proton, and Electron (HOPE) Mass Spectrometer (Funsten et al., 2013). Then, the power distribution of all the rays at MLAT = 18° close to the observation latitude is presented in Figure 3.

Figure 3 shows the results of ray tracing by a bulk of rays from a single source. The equatorial projections of the ray locations at MLAT = 18° in the three density models are shown as the scattered stars in Figures 3a–3c in Solar Magnetic (SM) Coordinates, respectively. The ϕ value of each ray is shown in color with a circular colormap. In the steep density model (Figure 3a), the eastward rays cannot enter the plume and are reflected back to the trough region, which agrees with the individual ray-tracing result (Figure 2a). The reflected rays with $\phi \sim 90°$ (eastward) cluster around the local time close to the source shown in the white dot (Figure 3a). In contrast, the westward rays are not affected by the steep density gradient (Figure 3a), and are at the same locations as in the density model with no azimuthal gradient (Figure 3c). In the smooth density model, the eastward rays propagate into the "smooth plume" and also cluster around $Y = 1.85\ R_E$ with $\phi \sim 90°$. The clustering of the very oblique rays within a finite local time is due to the small perpendicular group velocity when θ is close to the Gendrin angle θ_G. Most rays move to higher L-shells relative to the source (Figures 3a–3c). Figures 3d–3f show the power distribution in θ and ϕ space. In the model with no azimuthal density gradient (Figure 3f), the power distribution is primarily anti-Earthward with a peak of θ between 30° and 60° and is symmetric in the east-west direction, similar to the observations in the first two boxes (Figures 1e and 1f). In contrast, a strong eastward peak is shown in the steep density model at $\phi \sim 90°$ and $\theta \sim 90°$ (or the resonance cone angle), and the anti-Earthward peak is asymmetric with a weaker power on the eastward side (Figure 3d). In Figure 3d, the quasi-parallel ray powers at $\theta < 60°$ are averagely damped to 0.90 of their initial values, while the very oblique ray powers at $\theta > 70°$ are averagely damped to 0.52 of their initial values because of stronger Landau damping. However, the effect of Landau damping is overshadowed by the clustering of the very oblique, eastward rays in k space due to refraction and reflection. The power distribution in the smooth density model also has the very oblique, eastward peak, but strong power is presented in all values of ϕ from −20° to 90° (Figure 1e). The anti-Earthward peak is relatively weak (Figure 3e) because the azimuthal density gradient is presented near the source (Figure 3b) and also affects the westward propagating rays.

The power distributions from a single source are not enough to explain the observed distributions because of a larger area of the source region and a finite area of the satellite's observation. The source is extended in local times because the chorus at the same frequency as Figures 1c and 1d is observed since 17:40 (hh:mm) around MLT = 12.6 hr (not shown). Therefore, the power distributions in Figures 1e–1h possibly come from sources at different local times. As such, we conduct ray tracing from 61 sources at the same L shell at MLTs from 12.850 to 13.150 hr, with one source every 0.005 hr MLT. The initial wave normal and wave power distributions for each source and the damping calculations are the same as the single source ray tracing. The westmost source is at MLT = 12.850 hr because the eastward rays may propagate ∼ 0.25 hr MLT (Figure 2c) to reach the observed region near MLT = 13.1 hr (Figure 1c). Figures 4a–4d show the power distributions at MLAT = 18° and $5.2 < L < 5.4$ within the MLT ranges of each box in Figure 1c. The equatorial projection of each box where the power distributions are plotted is shown in Figure 3a. In Boxes 1–3, there is an anti-Earthward peak at θ between 30° and 60° (Figures 4a–4c). Compared to the observation power at θ between 10° and 40° (Figures 1e–1g), the peaks from ray-tracing are more oblique and incline slightly eastward. The discrepancy may be caused by a compressed magnetic field at dayside and an off-equatorial B minimum so that the sources may be closer to the satellite, resulting in less inclined k vectors and more westward rays coming from nearby sources. The difference could also be due to the real density profile along the magnetic field line being different from that used in the model. Box 4 presents a strong eastward and very oblique peak, and the high-power region extends along ϕ between 0° and 90° (Figure 4d), in agreement with Figure 1h. The extension of power along ϕ is the result of the spreading of

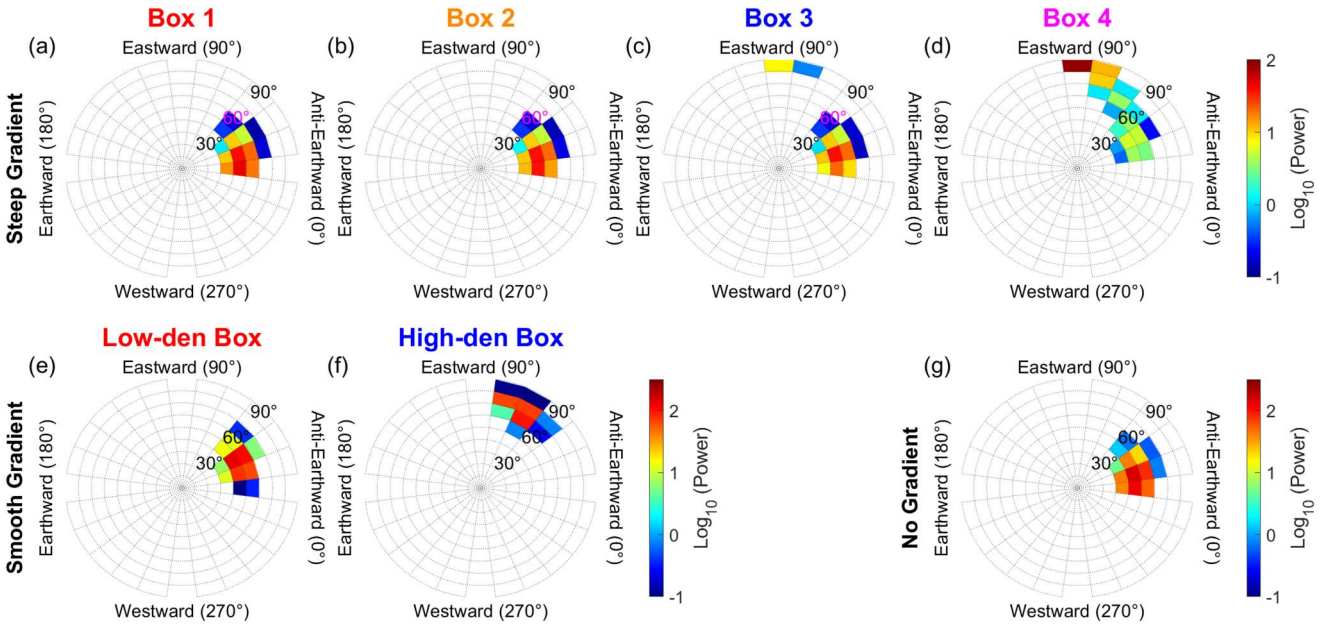

Figure 4. Results of power distribution from multiple sources at $L = 5.0$ from MLT = 12.850 hr to MLT = 13.150 hr (a)–(d) Power distribution in the steep density gradient model at MLAT = 18° and $5.2 < L < 5.4$ in the four boxes shown in Figure 3a, respectively. The MLT ranges of these boxes correspond to the four boxes shown in Figure 1c in the observation. (e)–(f) Power distribution in the steep density gradient model at MLAT = 18° in the two boxes shown in Figure 3b. (g) Power distribution in model with no azimuthal density gradient at MLAT = 18° in the black box shown in Figure 3c.

wave sources along different MLTs. In sum, the transformation in the ray-tracing results from Box 1 to Box 4 generally agrees with the observed trend in Figures 1e–1h. For comparison results in the smooth density model, we choose two boxes with a wider MLT range because the wave characteristics change slowly with MLT. We choose a box at a relatively low-density region covering all the area of the four boxes in the steep density model (red box in Figure 3b), and another box relatively high-density region with the same MLT width centering at 10% of the peak density enhancement value (blue box in Figure 3b). Figures 4e and 4f show the power distributions of the two boxes in the smooth density model. The anti-Earthward peak in the low-density box (Figure 4e) is similar to Box 1–3 in the steep density model. At higher density, there is only one very oblique and eastward power peak but no quasi-parallel power, which is different from the observation in Figure 1h and the model results with a steep azimuthal density gradient in Figure 4d. Figure 4g shows the power distribution of rays in the density model with no azimuthal gradient, measured in the same area as the low-density box for the smooth density model (black box in Figure 3c). The result is also similar to Box 1–3 in the steep density model, where most of the rays are not affected by the plume edge.

5. The Criterion for Low-Latitude Plume Entry

Past ray-tracing studies on the chorus-to-hiss mechanism have shown that chorus waves can enter the plume and into the plasmasphere (Chen et al., 2009; Hartley et al., 2019). However, for the observations presented above, the chorus waves do not enter the plume with a steep edge. In this section, we discuss the criterion for chorus waves to enter a steep azimuthal density structure (or plume) at low latitudes ($|MLAT| < 20°$). To simplify, we choose a chorus ray with initial $k_\perp$ directed azimuthally toward the plume. The ray is launched in the trough region with density N_0. Assuming the electron plasma frequency is much larger than the electron gyrofrequency $\left(\omega_{pe}^2 \gg \Omega_{ce}^2\right)$ and the wave frequency is much larger than the lower hybrid frequency $\left(\omega^2 \gg \Omega_{LH}^2\right)$, the cold plasma dispersion relation of whistler-mode waves can be simplified as (Lundin & Krafft, 2001):

$$D = \omega - \frac{\Omega_{ce}\cos\theta}{1 + (\omega_{pe}/kc)^2} = 0. \quad (2)$$

21699402, 2024, 2, Downloaded from https://agupubs.onlinelibrary.wiley.com/doi/10.1029/2023JA032151 by British Antarctic Survey, Wiley Online Library on [29/09/2025]. See the Terms and Conditions (https://onlinelibrary.wiley.com/terms-and-conditions) on Wiley Online Library for rules of use; OA articles are governed by the applicable Creative Commons License

21699402, 2024, 2, Downloaded from https://agupubs.onlinelibrary.wiley.com/doi/10.1029/2023JA032151 by British Antarctic Survey, Wiley Online Library on [29/09/2025]. See the Terms and Conditions (https://onlinelibrary.wiley.com/terms-and-conditions) on Wiley Online Library for rules of use; OA articles are governed by the applicable Creative Commons License

We assume $k_{\|}$, the parallel component of k, is nearly constant along the raypath at low latitudes, which is true in our ray tracing where the total change of $k_{\|}$ is within 30%. Thus, $k_{\|}$ can be expressed as its initial value:

$$k\| = \frac{\omega_{pe0}\cos\theta_0}{c}\sqrt{\frac{\omega}{\Omega_{ce}\cos\theta_0 - \omega}}, \tag{3}$$

where ω_{pe0} is the initial electron plasma frequency. If the ray is reflected at the plume edge, the wave normal angle must have reached the Gendrin angle θ_G at density N_G, where the perpendicular group velocity $v_{g\perp} = -\frac{\partial D}{\partial k_\perp}\frac{\partial D}{\partial \omega} = 0$. Assuming a small variation of background magnetic field and a constant Ω_{ce}, we have

$$k_G = \frac{\omega_{peG}}{c}, \quad \cos\theta_G = \frac{2\omega}{\Omega_{ce}}. \tag{4}$$

Then the electron plasma frequency at the reflection point is

$$\omega_{peG} = \frac{k\|c}{\cos\theta_G} = \frac{\omega_{pe0}\Omega_{ce}\cos\theta_0}{2}\frac{1}{\sqrt{(\Omega_{ce}\cos\theta_0 - \omega)\omega}}. \tag{5}$$

And we get the expression of the density at the reflection point:

$$N_G = \frac{\Omega_{ce}^2 cos^2\theta_0}{4\omega(\Omega_{ce}\cos\theta_0 - \omega)}N_0. \tag{6}$$

If the density inside the plume N_{pl} satisfies $N_{pl} > N_G$, the ray is reflected and cannot enter the plume. The ray can only enter the plume if the plume density is lower than the criterion N_G. For a typical 500 Hz ray with $\theta_0 = 30°$ in our observation, the plume density need to be smaller than ~2.9 times the trough density by Equation 5 if the ray can enter the plume, while the observed plume density is ~9 times the trough density. Equation 5 generally agrees with our ray-tracing results in the steep density model on N_G under frequencies from 300 Hz to 1 kHz and different θ_0 with an error of less than 15%. One should note that Equation 5 only applies to the equatorial region with $|MLAT| < 20°$, and the azimuthal range of the plume edge should be smaller than the azimuthal spread of the rays near the equatorial region, which is ~$0.2R_E$ in our case (Figure 3c). For a wider plume edge in the azimuthal direction as our smooth density model, the chorus wave can continue propagating azimuthally toward the plume (Figure 2b) until reaching high latitudes. The ray-tracing model used by Chen et al. (2009); Hartley et al. (2019) has a relatively smooth and wide plume edge, so the rays are not reflected away from the plume near the equator.

6. Conclusion and Discussions

We present an observation of chorus waves near the westward edge of a plasmaspheric plume. Ray tracing is used to simulate the behavior of wave power in the k space. Our results are as follows.

1. Close to the westward plume edge, observations show that the chorus wave becomes very oblique with the k vector directed eastward. Further away from the plume edge, the k vectors are directed to anti-Earthward.
2. Ray tracing shows that the plume's steep azimuthal density gradient strongly refracts the chorus wave at the plume edge.
3. The wave is reflected when the wave normal becomes larger than the Gendrin angle and thus cannot propagate into the plume. The wave can travel further into the density enhancement in a smoother density gradient.
4. Analytical criterion on plume density is established to determine if the chorus wave can enter the steep plume edge at low latitudes.

There is an eastward skew of the wave vector direction at the westward edge of the plume in our study. However, Hartley, Chen, et al. (2022) showed a generally eastward skew of k at the eastern edges of plumes, where the wave vector directions should move westward if affected by azimuthal density gradients, assuming the chorus source is east of the plume. Therefore, the phenomenon does not appear to be caused by the refraction of the azimuthal density gradient. We need further investigations on the possibility that the chorus waves at the eastern edges are generated obliquely.

21699402, 2024, 2, Downloaded from https://agupubs.onlinelibrary.wiley.com/doi/10.1029/2023JA032151 by British Antarctic Survey, Wiley Online Library on [29/09/2025]. See the Terms and Conditions (https://onlinelibrary.wiley.com/terms-and-conditions) on Wiley Online Library for rules of use; OA articles are governed by the applicable Creative Commons License

In this study, we assume the observed change of wave vector directions near the plume boundary is a spatial structure instead of a temporal structure, and that the wave sources in Figure 4 are uniformly distributed along the azimuthal direction. However, these assumptions may be undermined, as the observation time scale in our study, spanning 4 min, and the presumed spatial scale of wave sources, estimated at 2,500 km, considerably exceed the typical coherent chorus wave scales, which are around 10 s and 433 km, respectively (Zhang et al., 2021). Future studies might benefit from backward ray tracing, which can avoid these assumptions and pinpoint the source locations (Santolík et al., 2006).

The density gradient in this observation may actually be even steeper than our steep density model. During the narrowing of the plume, the western edge may move eastward at a fraction (15%–79%) of the local corotation speed (2.1 km/s in our case) (Spasojević et al., 2003; J. Goldstein et al., 2004), which is comparable to the satellite speed (2.8 km/s). This implies a possible steeper gradient of the spatial density structure. At 18:18:01 (hh:mm:ss), the very steep, $\sim$ 4 times density enhancement within 18 km is not manifested in our steep density model (Figure 1b). Considering that the parallel wavelength of 500 Hz is around 19 km, the WKB approximation is violated, and ray tracing cannot be applied to this density enhancement. Furthermore, only a purely azimuthal density gradient is considered in our density models. A smooth radial density gradient may direct the rays into lower L-shells. Despite the limitations above, our ray-tracing model still performs well in simulating the power distributions in k space.

Data Availability Statement

Data from Van Allen Probes can be assessed from https://cdaweb.gsfc.nasa.gov/. Ray-tracing results data can be downloaded from https://doi.org/10.5281/zenodo.8381779.

Acknowledgments
WG, DPH, and LC are supported by NASA grant 80NSSC20K1324. XL, LC, and JB are supported by NASA grant 80NSSC22K1637.

References

Agapitov, O. V., Artemyev, A., Krasnoselskikh, V., Khotyaintsev, Y. V., Mourenas, D., Breuillard, H., et al. (2013). Statistics of whistler mode waves in the outer radiation belt: Cluster staff-sa measurements. *Journal of Geophysical Research: Space Physics*, *118*(6), 3407–3420. https://doi.org/10.1002/jgra.50312

Agapitov, O. V., Mourenas, D., Artemyev, A. V., Mozer, F. S., Hospodarsky, G., Bonnell, J., & Krasnoselskikh, V. (2018). Synthetic empirical chorus wave model from combined van allen probes and cluster statistics. *Journal of Geophysical Research: Space Physics*, *123*(1), 297–314. https://doi.org/10.1002/2017JA024843

Artemyev, A., Agapitov, O., Mourenas, D., Krasnoselskikh, V., Shastun, V. V., & Mozer, F. (2016). Oblique whistler-mode waves in the earth's inner magnetosphere: Energy distribution, origins, and role in radiation belt dynamics. *Space Science Reviews*, *200*(1–4), 261–355. https://doi.org/10.1007/s11214-016-0252-5

Borovsky, J. E., & Denton, M. H. (2008). A statistical look at plasmaspheric drainage plumes. *Journal of Geophysical Research*, *113*(A9), A09221. https://doi.org/10.1029/2007JA012994

Bortnik, J., Chen, L., Li, W., Thorne, R. M., & Horne, R. B. (2011). Modeling the evolution of chorus waves into plasmaspheric hiss. *Journal of Geophysical Research*, *116*(A8), A08221. https://doi.org/10.1029/2011JA016499

Bortnik, J., Li, W., Thorne, R. M., Angelopoulos, V., Cully, C., Bonnell, J., et al. (2009). An observation linking the origin of plasmaspheric hiss to discrete chorus emissions. *Science*, *324*(5928), 775–778. https://doi.org/10.1126/science.1171273

Bortnik, J., Thorne, R. M., & Meredith, N. P. (2008). The unexpected origin of plasmaspheric hiss from discrete chorus emissions. *Nature*, *452*(7183), 62–66. https://doi.org/10.1038/nature06741

Bortnik, J., Thorne, R. M., Meredith, N. P., & Santolik, O. (2007). Ray tracing of penetrating chorus and its implications for the radiation belts. *Geophysical Research Letters*, *34*(15), L15109. https://doi.org/10.1029/2007GL030040

Burtis, W. J., & Helliwell, R. A. (1969). Banded chorus—A new type of vlf radiation observed in the magnetosphere by ogo 1 and ogo 3. *Journal of Geophysical Research*, *74*(11), 3002–3010. https://doi.org/10.1029/JA074i011p03002

Burton, R. K., & Holzer, R. E. (1974). The origin and propagation of chorus in the outer magnetosphere. *Journal of Geophysical*, *79*(7), 1014–1023. https://doi.org/10.1029/JA079i007p01014

Chen, L., Bortnik, J., Thorne, R. M., Horne, R. B., & Jordanova, V. K. (2009). Three-dimensional ray tracing of vlf waves in a magnetospheric environment containing a plasmaspheric plume. *Geophysical Research Letters*, *36*(22), L22101. https://doi.org/10.1029/2009GL040451

Chen, L., Thorne, R. M., Li, W., & Bortnik, J. (2013). Modeling the wave normal distribution of chorus waves. *Journal of Geophysical Research: Space Physics*, *118*(3), 1074–1088. https://doi.org/10.1029/2012JA018343

Darrouzet, F., De Keyser, J., Décréau, P. M. E., Gallagher, D. L., Pierrard, V., Lemaire, J. F., et al. (2006). Analysis of plasmaspheric plumes: Cluster and image observations. *Annales Geophysicae*, *24*(6), 1737–1758. https://doi.org/10.5194/angeo-24-1737-2006

Funsten, H. O., Skoug, R. M., Guthrie, A. A., MacDonald, E. A., Baldonado, J. R., Harper, R. W., et al. (2013). Helium, oxygen, proton, and electron (hope) mass spectrometer for the radiation belt storm probes mission. *Space Science Reviews*, *179*(1–4), 423–484. https://doi.org/10.1007/s11214-013-9968-7

Gao, X., Mourenas, D., Li, W., Artemyev, A. V., Lu, Q., Tao, X., & Wang, S. (2016). Observational evidence of generation mechanisms for very oblique lower band chorus using themis waveform data. *Journal of Geophysical Research: Space Physics*, *121*(7), 6732–6748. https://doi.org/10.1002/2016JA022915

Gendrin, R. (1961). Le guidage des whistlers par le champ magnetique. *Planetary and Space Science*, *5*(4), 274–282. https://doi.org/10.1016/0032-0633(61)90096-4

Goldstein, B. E., & Tsurutani, B. T. (1984). Wave normal directions of chorus near the equatorial source region. *Journal of Geophysical Research*, *89*(A5), 2789–2810. https://doi.org/10.1029/JA089iA05p02789

Goldstein, J., Sandel, B. R., Thomsen, M. F., Spasojević, M., & Reiff, P. H. (2004). Simultaneous remote sensing and in situ observations of plasmaspheric drainage plumes. *Journal of Geophysical Research*, *109*(A3), A03202. https://doi.org/10.1029/2003JA010281

Haque, N., Spasojevic, M., Santolík, O., & Inan, U. S. (2010). Wave normal angles of magnetospheric chorus emissions observed on the polar spacecraft. *Journal of Geophysical Research*, *115*(A4), A00F07. https://doi.org/10.1029/2009JA014717

Hartley, D. P., Chen, L., Christopher, I. W., Kletzing, C. A., Santolik, O., Li, W., & Shi, R. (2022). The angular distribution of lower band chorus waves near plasmaspheric plumes. *Geophysical Research Letters*, *49*(9), e2022GL098710. e2022GL098710 2022GL098710). https://doi.org/10.1029/2022GL098710

Hartley, D. P., Christopher, I. W., Kletzing, C. A., Kurth, W. S., Santolik, O., Kolmasova, I., et al. (2023). Chorus wave properties from van allen probes: Quantifying the impact of the sheath corrected electric field. *Geophysical Research Letters*, *50*(7), e2023GL102922. e2023GL102922 2023GL102922). https://doi.org/10.1029/2023GL102922

Hartley, D. P., Christopher, I. W., Kletzing, C. A., Kurth, W. S., Santolik, O., Kolmasova, I., et al. (2022b). Quantifying the sheath impedance of the electric double probe instrument on the van allen probes. *Journal of Geophysical Research: Space Physics*, *127*(5), e2022JA030369. https://doi.org/10.1029/2022JA030369

Hartley, D. P., Kletzing, C. A., Chen, L., Horne, R. B., & Santolík, O. (2019). Van allen probes observations of chorus wave vector orientations: Implications for the chorus-to-hiss mechanism. *Geophysical Research Letters*, *46*(5), 2337–2346. https://doi.org/10.1029/2019GL082111

Hartley, D. P., Kletzing, C. A., Santolík, O., Chen, L., & Horne, R. B. (2018). Statistical properties of plasmaspheric hiss from van allen probes observations. *Journal of Geophysical Research: Space Physics*, *123*(4), 2605–2619. https://doi.org/10.1002/2017JA024593

Helliwell, R. A. (1965). *Whistlers and related ionospheric phenomena*. Stanford University Press.

Hikishima, M., Omura, Y., & Summers, D. (2010). Microburst precipitation of energetic electrons associated with chorus wave generation. *Geophysical Research Letters*, *37*(7), L07103. https://doi.org/10.1029/2010GL042678

Horne, R. B. (1989). Path-integrated growth of electrostatic waves: The generation of terrestrial myriametric radiation. *Journal of Geophysical Research*, *94*(A7), 8895–8909. https://doi.org/10.1029/JA094iA07p08895

Horne, R. B., Thorne, R. M., Glauert, S. A., Albert, J. M., Meredith, N. P., & Anderson, R. R. (2005). Timescale for radiation belt electron acceleration by whistler mode chorus waves. *Journal of Geophysical Research*, *110*(A3), A03225. https://doi.org/10.1029/2004JA010811

Huang, C. Y., & Goertz, C. K. (1983). Ray-tracing studies and path-integrated gains of elf unducted whistler mode waves in the earth's magnetosphere. *Journal of Geophysical Research*, *88*(A8), 6181–6187. https://doi.org/10.1029/JA088iA08p06181

Kletzing, C. A., Bortnik, J., Hospodarsky, G., Kurth, W. S., Santolik, O., Smith, C. W., et al. (2023). The electric and magnetic fields instrument suite and integrated science (emfisis): Science, data, and usage best practices. *Space Science Reviews*, *219*(28), 28. https://doi.org/10.1007/s11214-023-00973-z

Kletzing, C. A., Kurth, W. S., Acuna, M., MacDowall, R. J., Torbert, R. B., Averkamp, T., et al. (2013). The electric and magnetic field instrument suite and integrated science (emfisis) on rbsp. *Space Science Reviews*, *179*(1), 127–181. https://doi.org/10.1007/s11214-013-9993-6

Kurth, W. S., De Pascuale, S., Faden, J. B., Kletzing, C. A., Hospodarsky, G. B., Thaller, S., & Wygant, J. R. (2015). Electron densities inferred from plasma wave spectra obtained by the waves instrument on van allen probes. *Journal of Geophysical Research: Space Physics*, *120*(2), 904–914. https://doi.org/10.1002/2014JA020857

Lauben, D. S., Inan, U. S., Bell, T. F., & Gurnett, D. A. (2002). Source characteristics of elf/vlf chorus. *Journal of Geophysical Research*, *107*(A12), 1429. https://doi.org/10.1029/2000JA003019

LeDocq, M. J., Gurnett, D. A., & Hospodarsky, G. B. (1998). Chorus source locations from vlf poynting flux measurements with the polar spacecraft. *Geophysical Research Letters*, *25*(21), 4063–4066. https://doi.org/10.1029/1998GL900071

Li, J., Bortnik, J., An, X., Li, W., Angelopoulos, V., Thorne, R. M., et al. (2019). Origin of two-band chorus in the radiation belt of earth. *Nature Communications*, *10*(4672), 4672. https://doi.org/10.1038/s41467-019-12561-3

Li, W., Bortnik, J., Thorne, R. M., Cully, C. M., Chen, L., Angelopoulos, V., et al. (2013). Characteristics of the poynting flux and wave normal vectors of whistler-mode waves observed on themis. *Journal of Geophysical Research: Space Physics*, *118*(4), 1461–1471. https://doi.org/10.1002/jgra.50176

Li, W., Santolik, O., Bortnik, J., Thorne, R. M., Kletzing, C. A., Kurth, W. S., & Hospodarsky, G. B. (2016). New chorus wave properties near the equator from van allen probes wave observations. *Geophysical Research Letters*, *43*(10), 4725–4735. https://doi.org/10.1002/2016GL068780

Liu, X., & Chen, L. (2019). Instability in a relativistic magnetized plasma. *Physics of Plasmas*, *26*(4), 042902. https://doi.org/10.1063/1.5089749

Liu, X., Gu, W., Xia, Z., Chen, L., & Horne, R. B. (2021). Frequency-dependent modulation of whistler-mode waves by density irregularities during the recovery phase of a geomagnetic storm. *Geophysical Research Letters*, *48*(16), e2021GL093095. e2021GL093095 2021GL093095. https://doi.org/10.1029/2021GL093095

Lu, Q., Ke, Y., Wang, X., Liu, K., Gao, X., Chen, L., & Wang, S. (2019). Two-dimensional gcpic simulation of rising-tone chorus waves in a dipole magnetic field. *Journal of Geophysical Research: Space Physics*, *124*(6), 4157–4167. https://doi.org/10.1029/2019JA026586

Lundin, B., & Krafft, C. (2001). On the similarity features of normalized frequency spectrograms of magnetospherically reflected whistlers. *Journal of Geophysical Research*, *106*(A11), 25643–25654. https://doi.org/10.1029/2000JA000346

Ma, J., Gao, X., Chen, H., Tsurutani, B. T., Ke, Y., Chen, R., & Lu, Q. (2022). The effects of substorm injection of energetic electrons and enhanced solar wind ram pressure on whistler-mode chorus waves: A statistical study. *Journal of Geophysical Research: Space Physics*, *127*(11), e2022JA030502. (e2022JA030502 2022JA030502). https://doi.org/10.1029/2022JA030502

Meredith, N. P., Horne, R. B., Shen, X.-C., Li, W., & Bortnik, J. (2020). Global model of whistler mode chorus in the near-equatorial region ($|\lambda_m| < 18°$). *Geophysical Research Letters*, *47*(11), e2020GL087311. https://doi.org/10.1029/2020GL087311

Mourenas, D., Artemyev, A., Agapitov, O., & Krasnoselskikh, V. (2012). Acceleration of radiation belts electrons by oblique chorus waves. *Journal of Geophysical Research*, *117*(A10), A10212. https://doi.org/10.1029/2012JA018041

Nishimura, Y., Bortnik, J., Li, W., Thorne, R. M., Chen, L., Lyons, L. R., et al. (2011). Multievent study of the correlation between pulsating aurora and whistler mode chorus emissions. *Journal of Geophysical Research*, *116*(A11), A11221. https://doi.org/10.1029/2011JA016876

Omura, Y., Katoh, Y., & Summers, D. (2008). Theory and simulation of the generation of whistler-mode chorus. *Journal of Geophysical Research*, *113*(A4), A04223. https://doi.org/10.1029/2007JA012622

Santolík, O., Chum, J., Parrot, M., Gurnett, D. A., Pickett, J. S., & Cornilleau-Wehrlin, N. (2006). Propagation of whistler mode chorus to low altitudes: Spacecraft observations of structured elf hiss. *Journal of Geophysical Research*, *111*(A10), A10208. https://doi.org/10.1029/2005JA011462

Santolík, O., Parrot, M., & Lefeuvre, F. (2003). Singular value decomposition methods for wave propagation analysis. *Radio Science*, *38*(1), 1010. https://doi.org/10.1029/2000RS002523

Shi, R., Mourenas, D., Artemyev, A., Li, W., & Ma, Q. (2018). Highly oblique lower-band chorus statistics: Dependencies of wave power on refractive index and geomagnetic activity. *Journal of Geophysical Research: Space Physics*, *123*(6), 4767–4784. https://doi.org/10.1029/2018JA025337

21699402, 2024, 2, Downloaded from https://agupubs.onlinelibrary.wiley.com/doi/10.1029/2023JA032151 by British Antarctic Survey, Wiley Online Library on [29/09/2025]. See the Terms and Conditions (https://onlinelibrary.wiley.com/terms-and-conditions) on Wiley Online Library for rules of use; OA articles are governed by the applicable Creative Commons License

Shprits, Y. Y., & Ni, B. (2009). Dependence of the quasi-linear scattering rates on the wave normal distribution of chorus waves. *Journal of Geophysical Research*, *114*(A11), A11205. https://doi.org/10.1029/2009JA014223

Spasojević, M., Goldstein, J., Carpenter, D. L., Inan, U. S., Sandel, B. R., Moldwin, M. B., & Reinisch, B. W. (2003). Global response of the plasmasphere to a geomagnetic disturbance. *Journal of Geophysical Research*, *108*(A9), 1340. https://doi.org/10.1029/2003JA009987

Stix, T. A. (1992). *Wavea in plasmas*. American Institute of Physics.

Tao, X. (2014). A numerical study of chorus generation and the related variation of wave intensity using the dawn code. *Journal of Geophysical Research: Space Physics*, *119*(5), 3362–3372. https://doi.org/10.1002/2014JA019820

Taubenschuss, U., Khotyaintsev, Y. V., Santolík, O., Vaivads, A., Cully, C. M., Contel, O. L., & Angelopoulos, V. (2014). Wave normal angles of whistler mode chorus rising and falling tones. *Journal of Geophysical Research: Space Physics*, *119*(12), 9567–9578. https://doi.org/10.1002/2014JA020575

Taubenschuss, U., Santolík, O., Breuillard, H., Li, W., & Le Contel, O. (2016). Poynting vector and wave vector directions of equatorial chorus. *Journal of Geophysical Research: Space Physics*, *121*(12), 912–928. https://doi.org/10.1002/2016JA023389

Teng, S., Tao, X., & Li, W. (2019). Typical characteristics of whistler mode waves categorized by their spectral properties using van allen probes observations. *Geophysical Research Letters*, *46*(7), 3607–3614. https://doi.org/10.1029/2019GL082161

Teng, S., Tao, X., Xie, Y., Zonca, F., Chen, L., Fang, W. B., & Wang, S. (2017). Analysis of the duration of rising tone chorus elements. *Geophysical Research Letters*, *44*(24), 074–082. https://doi.org/10.1002/2017GL075824

Thorne, R. M., Ni, B., Tao, X., Horne, R. B., & Meredith, N. P. (2010). Scattering by chorus waves as the dominant cause of diffuse auroral precipitation. *Nature*, *467*(7318), 943–946. https://doi.org/10.1038/nature09467

Trakhtengerts, V. Y. (1995). Magnetosphere cyclotron maser: Backward wave oscillator generation regime. *Journal of Geophysical Research*, *100*(A9), 17205–17210. https://doi.org/10.1029/95JA00843

Tsurutani, B. T., Lakhina, G. S., & Verkhoglyadova, O. P. (2013). Energetic electron (>10 kev) microburst precipitation, ∼5–15 s x-ray pulsations, chorus, and wave-particle interactions: A review. *Journal of Geophysical Research: Space Physics*, *118*(5), 2296–2312. https://doi.org/10.1002/jgra.50264

Tsurutani, B. T., & Smith, E. J. (1974). Postmidnight chorus: A substorm phenomenon. *Journal of Geophysical Research*, *79*(1), 118–127. https://doi.org/10.1029/JA079i001p00118

Wu, Z., Su, Z., Goldstein, J., Liu, N., He, Z., Zheng, H., & Wang, Y. (2022). Nightside plasmaspheric plume-to-core migration of whistler-mode hiss waves. *Geophysical Research Letters*, *49*(16), e2022GL100306. https://doi.org/10.1029/2022GL100306

Xiao, F., Yang, C., He, Z., Su, Z., Zhou, Q., He, Y., et al. (2014). Chorus acceleration of radiation belt relativistic electrons during march 2013 geomagnetic storm. *Journal of Geophysical Research: Space Physics*, *119*(5), 3325–3332. https://doi.org/10.1002/2014JA019822

Xie, Y., Teng, S., Wu, Y., & Tao, X. (2021). A statistical analysis of duration and frequency chirping rate of falling tone chorus. *Geophysical Research Letters*, *48*(19), e2021GL095349. (e2021GL095349 2021GL095349). https://doi.org/10.1029/2021GL095349

Zhang, S., Rae, I. J., Watt, C. E. J., Degeling, A. W., Tian, A., Shi, Q., et al. (2021). Determining the global scale size of chorus waves in the magnetosphere. *Journal of Geophysical Research: Space Physics*, *126*(11), e2021JA029569. (e2021JA029569 2021JA029569). https://doi.org/10.1029/2021JA029569

21699402, 2024, 2, Downloaded from https://agupubs.onlinelibrary.wiley.com/doi/10.1029/2023JA032151 by British Antarctic Survey, Wiley Online Library on [29/09/2025]. See the Terms and Conditions (https://onlinelibrary.wiley.com/terms-and-conditions) on Wiley Online Library for rules of use; OA articles are governed by the applicable Creative Commons License